Intermittent Fasting Activates AMP-Kinase to Restructure Right Ventricular Lipid Metabolism and Microtubules in Rodent Pulmonary Arterial Hypertension

Felipe Kazmirczak, MD[1], Sasha Z. Prisco, MD, PhD[1,2], Lynn M. Hartweck, PhD[2], and Kurt W. Prins, MD, PhD[1,2]

1. Cardiovascular Division, Department of Medicine, University of Minnesota Medical School, Minneapolis, MN
2. Lillehei Heart Institute, University of Minnesota Medical School, Minneapolis, MN

Funding: SZP is funded by NIH F32 HL154533 and a University of Minnesota Clinical and Translational Science award (NIH UL1 TR002494). KWP was funded by NIH K08 HL140100, the University of Minnesota Futures Grant, the University of Minnesota Faculty Research Development Grant Program, an Innovation Grant from the American Lung Association (IA-816386), and the Cardiovascular Medical Research and Education Fund.

Author for Correspondence

Kurt Prins, MD, PhD

Assistant Professor of Medicine

Lillehei Heart Institute

Cardiovascular Division

University of Minnesota Medical School

Minneapolis, MN 5545

Email: prin0088@umn.edu

Abstract

Intermittent fasting (IF) extends lifespan via pleotropic mechanisms, but one important molecular mediator of the beneficial effects of IF is AMP-kinase (AMPK). AMPK enhances lipid metabolism and modulates microtubule dynamics. Dysregulation of these two molecular pathways causes right ventricular (RV) failure in pulmonary arterial hypertension (PAH). In rodent PAH, IF activates RV AMPK, which restores mitochondrial and peroxisomal density and restructures mitochondrial and peroxisomal lipid metabolism protein regulation. In addition, IF increases electron transport chain (ETC) protein abundance and activity in the RV. Echocardiographic and hemodynamic measures of RV function are positively associated with fatty acid oxidation and ETC protein levels in correlational heatmapping analyses. IF also combats heightened microtubule density, which normalizes t-tubule structure. In summation, we demonstrate IF-mediated AMPK signaling counteracts two key molecular drivers of RV failure. Thus, IF may be a novel treatment approach for RV dysfunction, a currently untreatable and lethal consequence of PAH.

IF is a powerful life-prolonging intervention as numerous studies demonstrate IF confers survival benefits in multiple species and in several disease models[1,2]. One of the numerous biological benefits of IF is advantageous metabolic reprogramming[1]. *C. elegans* studies show AMPK signaling specifically underlies the lifespan-extending properties of IF via augmentation of fatty acid oxidation[3]. In particular, IF prevents the age-related decline in mitochondria and peroxisomes, and thereby enhances lipid metabolism[3].

RV failure is the leading cause of death in PAH, and unfortunately there are no effective therapies that directly enhance RV function[4]. Multiple laboratories have linked impaired fatty acid oxidation and altered lipid metabolism to RV dysfunction in PAH[5]. Both preclinical models[6,7] and human data[8] demonstrate increased levels of toxic ceramides in the RV, which can be a consequence of disrupted mitochondrial fatty acid degradation[9]. We recently showed IF combats lipotoxicity as there is an attenuation of ceramide accumulation in the RV of the monocrotaline (MCT) rat model of PAH[10]. Thus, IF may enhance or even restructure RV lipid metabolism, but an in-depth molecular characterization of the effects of IF on RV mitochondrial and peroxisomal lipid handling and metabolizing enzymes is lacking.

In addition to AMPK's well documented metabolic effects, AMPK also regulates microtubule dynamics via phosphorylation of the microtubule-associated proteins, microtubule associated protein-4 (MAP4)[11] and cytoplasmic linker protein-170 (CLIP170)[12]. Phosphorylation of MAP4 and CLIP170 reduces their microtubule binding affinity, which ultimately alters microtubule stability. There is strong evidence that increased microtubule density/stability compromises cardiac function via multiple mechanisms[13,14]. We and others show microtubule remodeling results in disrupted transverse-tubule (t-tubule) structure and function via dysregulation of junctophilin-2[15,16]. However, the impact of IF on MAP4 and CLIP170 phosphorylation states and the subsequent effects on microtubule regulation and t-tubule architecture have not been explored.

We first evaluated how IF modulated AMPK activation in the RV in the MCT model of RV failure. Immunoblots revealed MCT rats allowed to eat *ad libitum* (MCT-*ad lib*) had blunted AMPK signaling with lower levels of phosphorylated AMPK. However, IF activated AMPK as demonstrated by a significant increase in the levels of phosphorylated AMPK (pAMPK) and the ratio of pAMK to total AMPK as compared to MCT-*ad lib* animals (**Figure 1A and B**). Because AMPK regulates mitochondria and peroxisomal form and function[3], we used confocal microscopy to evaluate how IF impacted mitochondria/peroxisomal density in RV cardiomyocytes. When compared to controls, MCT-*ad lib* animals had reduced mitochondrial density, which IF

mitigated (**Figure 1C and Supplemental Video 1-3**). When evaluating RV cardiomyocyte peroxisomes, we observed a significant increase in peroxisomal density in MCT-*ad lib* animals, but IF blunted this abnormal response (**Figure 1D and Supplemental Video 4-6**). To understand how these morphological changes were related to fatty acid metabolic protein regulation, we performed quantitative proteomics profiling of RV mitochondrial and peroxisomal enrichments. Hierarchical cluster analysis demonstrated MCT rats had a distinct mitochondrial fatty acid proteomic signature as compared to controls. There were higher levels of the Acyl-CoA Synthetase Long Chain (ACSL) family of proteins in MCT-*ad lib* RVs, but lower levels of nearly all proteins responsible for fatty acid degradation including both units of the trifunctional enzyme (HADHA and HADHB) and multiple acyl-CoA dehydrogenase (ACAD) family members (**Figure 1E**). However, IF prevented the upregulation of ACSL proteins and downregulation of HADHA/HADHB and multiple ACAD proteins (**Figure 1E**). When peroxisomal α- and β-oxidation proteins were profiled, we observed differences between controls and MCT-*ad lib*, which was again abrogated by IF (**Figure 1F**). In MCT-*ad lib* RVs, multiples enzymes responsible for the import, export, and degradation of lipid species were upregulated. Interestingly, not all peroxisomal fatty acid metabolizing enzymes were increased in MCT-*ad lib* RVs as phytanoyl-CoA 2-hydroxylase (PHYH), L-bifunctional enzyme (EHHADH), sterol carrier protein 2 (SCP2), and peroxisome 3-ketoacyl-CoA thiolase (ACAA1) had decreased abundance in MCT-*ad lib* animals (**Figure 1F**). These results suggested both mitochondrial and peroxisomal fatty acid metabolic pathways were reprogramed in RV dysfunction, and that IF partially negated these responses.

In order to harness the energetic potential of fatty acid oxidation, the electron transport chain needs to convert NADH and $FADH_2$ into ATP[17]. Therefore, we examined the effects of IF on electron transport chain protein abundance and function. MCT-*ad lib* RVs had a distinct proteomic signature as compared to controls when each electron transport chain complex subunit was profiled. Hierarchical cluster analyses of all five electron transport chain complexes showed IF animals clustered with controls as IF prevented the downregulation of multiple electron transport chain subunit proteins that was observed in MCT-*ad lib* rats (**Figure 2A-E**). Next, we quantified electron transport chain activity using a recently developed Seahorse-based assay[18]. Complex I and Complex II oxygen consumption rates were reduced in MCT-*ad lib* RVs, but IF normalized the oxygen consumption rates of both complexes (**Figure 2F and G**). Complex IV activity was not significantly different between the three groups, however the sum of all three complexes was depressed in

MCT-*ad lib* but restored by IF (**Figure 2H and I**). Thus, these data demonstrated IF corrected RV electron transport chain protein regulation and activity.

Next, we used correlational heatmapping to interrogate the relationships between tricuspid plane annular systolic excursion (TAPSE), pressure-volume loop derived right ventricular-pulmonary artery coupling (Ees/Ea), and fatty acid oxidation and electron transport chain protein abundance. We observed significant and positive correlations between multiple mitochondrial fatty acid oxidation proteins with TAPSE and Ees/Ea (**Figure 3A-D**). However, ACSL4/5 protein abundance was inversely associated with RV function (**Figure 3A-D**). Peroxisomal fatty acid proteins also significantly correlated with RV function. Interestingly, enzymes responsible for fatty acid degradation were associated with better RV function, but proteins that modulate lipid uptake were negatively associated with RV function (**Figure 3E-H**). Finally, we showed positive correlations between multiple electron transport chain proteins in all five complexes and RV function (**Figure 3I-L**).

Then, we evaluated how AMPK activation modulated the microtubule cytoskeleton in RV failure. Western blot analysis revealed higher levels of the microtubule subunit proteins, α- and β-tubulin, in MCT-*ad lib* RVs, which was prevented by IF (**Figure 4A and B**). To determine if altered phosphorylation patterns of MAP4 and CLIP170 contributed to normalization of tubulin regulation, we probed total and phosphorylated levels of each protein in RV extracts. Both total CLIP170 and MAP4 were elevated in MCT-*ad lib* RVs, which IF combatted (**Figure 4A and B**). The three groups showed no differences in the ratio of phosphorylated CLIP170/total CLIP170, but the pMAP4/MAP4 ratio in the MCT-*ad lib* RVs was significantly depressed, which IF partially, but nonsignificantly corrected (**Figure 4A and B**). Then, we used confocal microscopy to quantify microtubule structure in RV cardiomyocytes. MCT-*ad lib* microtubule lattice density was significantly increased as compared to controls, but IF blunted microtubule proliferation (**Figure 4C and D**). Finally, we evaluated the downstream effects of microtubule dysregulation by probing junctophilin-2 protein abundance and t-tubule structure. Consistent with our previous work[15,19], junctophilin-2 levels were lower (**Figure 4A and B**) and t-tubule morphology was deranged in MCT-*ad lib* RV cardiomyocytes (**Figure 4 E and F**). However, in MCT-IF rats, junctophilin-2 levels were normalized (**Figure 4 A and B**) and t-tubule architecture was restored (**Figure 4E and F**).

In our correlational analyses, we observed an inverserelationship between ACSL4/5 and RV function, which requires further discussion and exploration. ACSL4/5 regulate ferroptosis[20,21], a nonapoptotic form of cell death linked to alterations in lipid metabolism[22]. To understand how ferroptosis may modulate RV function in PAH, we probed ferroptotic protein regulation and the relationships between ferroptosis proteins and TAPSE and Eea/Ea. Hierarchical cluster analysis showed MCT-*ad lib* had higher levels of pro-ferroptotic proteins than control animals, and the overall pattern of ferroptotic-regulating proteins was distinct (**Supplemental Figure 1A**). However, IF animals had a ferroptosis molecular signature that was similar to control with less upregulation of pro-ferroptotic enzymes (**Supplemental Figure 1A**). When performing correlational heatmapping, we found pro-ferroptotic proteins were negatively associated with RV function with one exception: Raf kinase inhibitor protein (RKIP/PEBP1) (**Supplemental Figure 1**). Consistent with our findings, PEBP1 directly augments cardiac contractility via modulation of beta-adrenergic signaling[23], and perhaps the positive inotropic effect of PEBP1 is more important than its ferroptosis function in diseased states. In summation, these results suggest another effect of IF is antagonism of ferroptosis. It is very possible the anti-ferroptotic effect of IF is also mediated by AMPK because AMPK suppresses ferroptosis in cancer cells and in renal ischemia-reperfusion by reprogramming lipid metabolism[24].

To the best of our knowledge, this study is the first to interrogate the effects of IF on ferroptosis protein regulation and cardiac function. However, our finding that a pro-ferroptosis state is associated with depressed cardiac contractility is congruent with results by other groups. First, small molecule inhibition of ferroptosis combats both doxorubicin and ischemia-reperfusion mediated left ventricular dysfunction[25]. Interestingly, the dampening of ferroptosis restores Complex I and II activity[25], which is consistent with our observation that conditions of heightened ferroptosis result in impaired Complex I and II function. Second, suppression of ferroptosis via glutathione peroxidase 4, a protein that reverses lipid peroxidation and blunts ferroptosis induction, overexpression mitigates doxorubicin cardiomyopathy[26]. Furthermore, mice with reduced glutathione peroxidase 4 expression have worse cardiac function after doxorubin exposure[26]. The combination of these two publications and our data show excess ferroptosis promotes cardiac dysfunction. Certainly, future studies examining the effects of ferroptosis inhibition in RV failure due to PAH would be helpful to determine if this pathway may be a novel therapeutic target.

Our current findings of peroxisomal remodeling in the setting of RV dysfunction agree with our previous work[7], but the consequences of these observations are unknown. However, the association between increased peroxisomal abundance and RV dysfunction along with the fact that many peroxisomal proteins are inversely correlated with RV function implies peroxisomal reprogramming may be maladaptive. A potential mechanism for this hypothesis could also be ferroptosis induction as a large CRISPR-based screen identified multiple peroxisomal proteins have the capacity to modulate ferroptosis sensitivity[27]. A series of well executed experiments revealed the synthesis of polyunsaturated ether phospholipids through the peroxisomal enzymes fatty acyl-CoA reductase 1 (FAR1), glyceronephosphate *O*-acyltransferase (GNPAT), and alkylglycerone phosphate synthase (AGPS) and the endoplasmic reticulum enzyme 1-acylglycerol-3-phosphate *O*-acyltransferase 3 (AGPAT3) drives the peroxisomal-ferroptotic pathway[27]. When we profiled these particular proteins in our proteomics experiments, we found increased abundance of all enzymes in MCT-*ad lib* RV (**Supplemental Figure 2**). IF partially suppressed the upregulation of all of these proteins, and hierarchical cluster analysis demonstrated MCT-IF rats had a similar peroxisomal-ferroptotic signature to controls animals (**Supplemental Figure 2**). Interestingly, all peroxisomal-ferroptotic pathway enzymes were inversely associated with RV function, and in particular, AGPS had the strongest association with RV dysfunction (**Supplemental Figure 2**). In conclusion, our study raises the possibility that increased peroxisomal density and the associated changes in enzymatic regulation may have deleterious effects on RV function via a newly described peroxisomal-ferroptotic pathway.

Our manuscript has important limitations that we must acknowledge. First, IF has pleiotropic effects including restoring circadian rhythm, restructuring the gut microbiome, and systemic anti-inflammatory effects[1,2,28]. Therefore, it is unlikely that the modulation of RV lipid metabolism and microtubule density are the only molecular mechanisms underlying improved RV function. Second, our proteomics experiments were conducted using whole RV free wall specimens and thus nonmuscle cells may contribute to some of the findings. Finally, we were unable to calculate Ees/Ea in all animals during catheterization (n=1 MCT-ad lib and n=1 MCT-IF), which may have explained where some of the correlational relationships were less significant than those observed with TAPSE.

Acknowledgements

The authors would like to thank Drs. LeeAnn Higgins and Todd Markowski of the University of Minnesota Center for Mass Spectrometry and Proteomics for assistance with our proteomics experiments. We would also like to thank Dr. Keita Uchida for sharing his antigen retrieval protocol for cardiomyocyte microtubule imaging. Finally, we would like to thank Dr. Yasunori Shintani for generously sharing the phospho-CLIP170 antibody.

Figure 1: Intermittent fasting activates AMPK signaling and restructures mitochondrial and peroxisomal density and lipid metabolism. (A) Representative Western blots of total AMPK and phosphorylated AMPK from RV extracts. CBB is Coomassie brilliant blue stained gel in the area of the myosin heavy chain. (B) Quantification of relative protein abundance. IF significantly increased pAMPK and pAMK/AMPK, consistent with an AMPK activating effect. *p*-values as determined by Kruskal-Wallis test with Dunn's multiple comparisons test. (C) Representative three-dimensional reconstructions of confocal micrographs of RV cardiomyocytes stained with mitofusin-2 (green), WGA (red), and DAPI (blue) to show mitochondrial density at low (left) or high magnification (right). Arrows highlight areas of reduced mitochondrial density in MCT-*ad lib* RV cardiomyocytes. Quantification of mitochondrial density in RV cardiomyocytes showed IF restored mitochondrial density. *p*-values as determined by one-way ANOVA with Tukey's multiple comparisons test. (D) Representative three-dimensional reconstructions of confocal micrographs of RV cardiomyocytes stained with catalase antibody (green), WGA (red), and DAPI (blue) showing cardiomyocyte peroxisomes. IF prevented the increase in peroxisomal density. *p*-values as determined by one-way ANOVA with Tukey's multiple comparisons test.

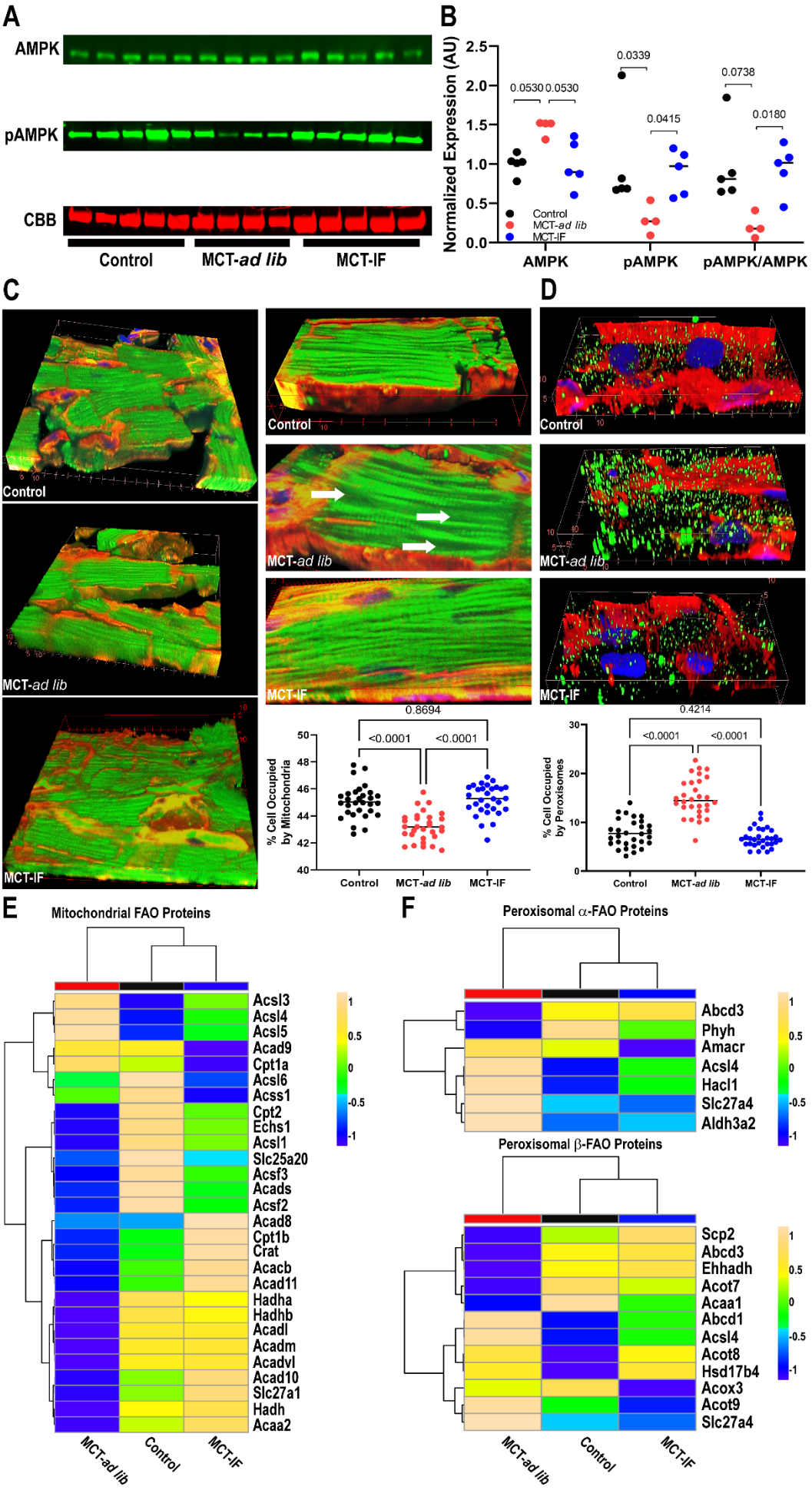
A
AMPK
pAMPK
CBB
Control
MCT-ad lib
MCT-IF
B
Normalized Expression (AU)
2.5
2.0
1.5
1.0
0.5
0.0
0.0530
0.0530
0.0339
0.0415
0.0738
0.0180
Control
MCT-ad lib
MCT-IF
AMPK
pAMPK
pAMPK/AMPK
C
Control
MCT-ad lib
MCT-IF
D
Control
MCT-ad lib
MCT-IF
0.8694
<0.0001
<0.0001
% Cell Occupied by Mitochondria
50
48
46
44
42
40
Control
MCT-ad lib
MCT-IF
0.4214
<0.0001
<0.0001
% Cell Occupied by Peroxisomes
30
20
10
0
Control
MCT-ad lib
MCT-IF
E
Mitochondrial FAO Proteins
Acsl3
Acsl4
Acsl5
Acad9
Cpt1a
Acsl6
Acss1
Cpt2
Echs1
Acsl1
Slc25a20
Acsf3
Acads
Acsf2
Acad8
Cpt1b
Crat
Acacb
Acad11
Hadha
Hadhb
Acadl
Acadm
Acadvl
Acad10
Slc27a1
Hadh
Acaa2
1
0.5
0
-0.5
-1
MCT-ad lib
Control
MCT-IF
F
Peroxisomal α-FAO Proteins
Abcd3
Phyh
Amacr
Acsl4
Hacl1
Slc27a4
Aldh3a2
1
0.5
0
-0.5
-1
Peroxisomal β-FAO Proteins
Scp2
Abcd3
Ehhadh
Acot7
Acaa1
Abcd1
Acsl4
Acot8
Hsd17b4
Acox3
Acot9
Slc27a4
1
0.5
0
-0.5
-1
MCT-ad lib
Control
MCT-IF

Figure 2: Intermittent fasting prevented dysregulation of electron transport chain protein subunits and enhanced electron transport chain function. Hierarchical cluster analyses of proteomic-derived abundance of proteins in Complex I (A), Complex II (B), Complex III (C), Complex IV (D), and Complex V (E). Intermittent fasting prevents dysregulation of all ETC complexes. Quantification of Complex I (F), Complex II (G), Complex IV (H), and combined Complex I, II, and IV (I) activity of frozen RV extracts. Intermittent fasting augmented electron transport chain function. *p*-values as determined by one-way ANOVA with Tukey's multiple comparisons test.

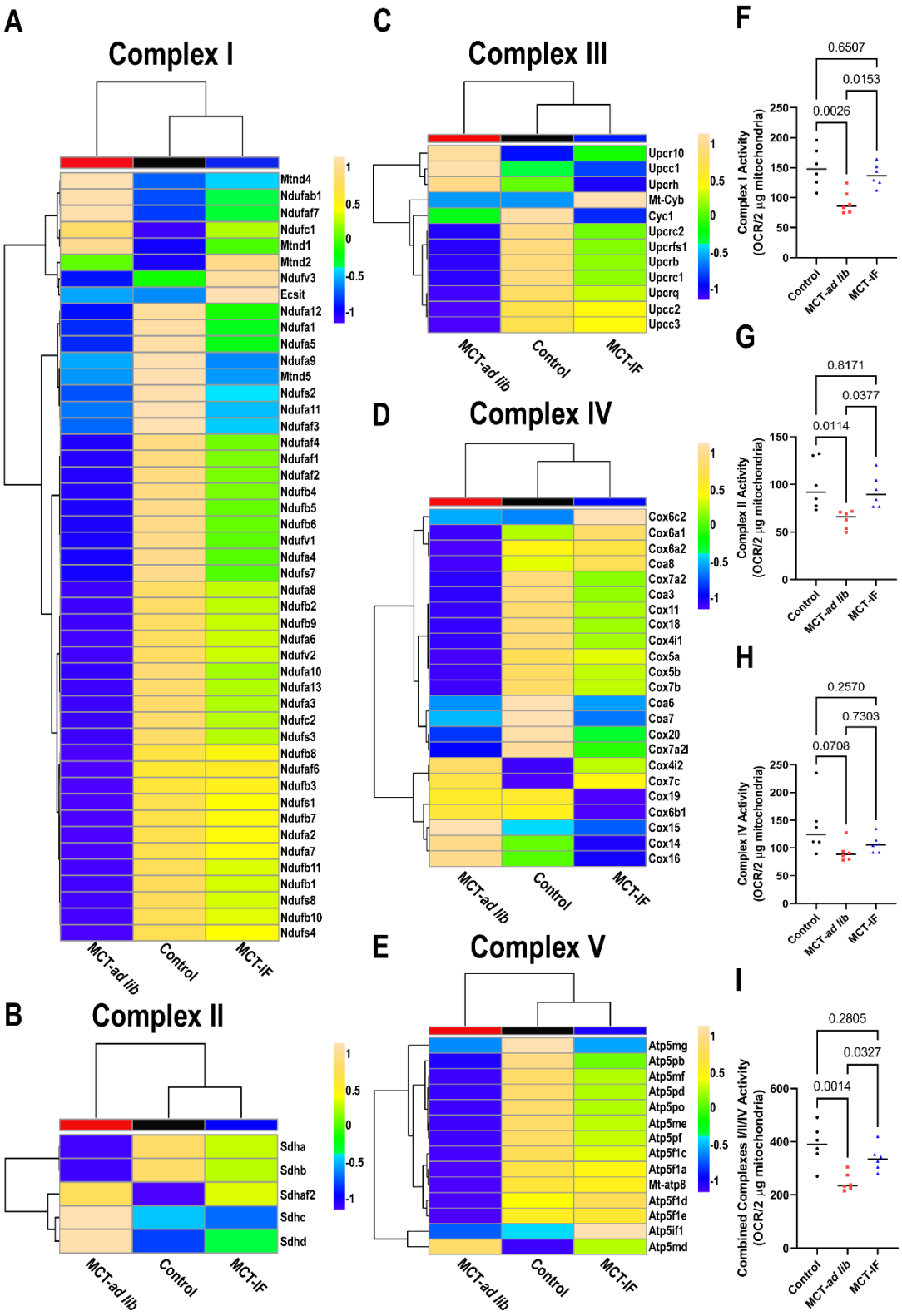
A
Complex I
Mtnd4
Ndufab1
Ndufaf7
Ndufc1
Mtnd1
Mtnd2
Ndufv3
Ecsit
Ndufa12
Ndufa1
Ndufa5
Ndufa9
Mtnd5
Ndufs2
Ndufa11
Ndufaf3
Ndufaf4
Ndufaf1
Ndufaf2
Ndufb4
Ndufb5
Ndufb6
Ndufv1
Ndufa4
Ndufs7
Ndufa8
Ndufb2
Ndufb9
Ndufa6
Ndufv2
Ndufa10
Ndufa13
Ndufa3
Ndufc2
Ndufs3
Ndufb8
Ndufaf6
Ndufb3
Ndufs1
Ndufb7
Ndufa2
Ndufa7
Ndufb11
Ndufb1
Ndufs8
Ndufb10
Ndufs4
MCT-ad libb
Control
MCT-IF
1
0.5
0
-0.5
-1
B
Complex II
Sdha
Sdhb
Sdhaf2
Sdhc
Sdhd
MCT-ad libb
Control
MCT-IF
C
Complex III
Upcr10
Upcc1
Upcrh
Mt-Cyb
Cyc1
Upcrc2
Upcrfs1
Upcrb
Upcrc1
Upcrq
Upcc2
Upcc3
MCT-ad libb
Control
MCT-IF
D
Complex IV
Cox6c2
Cox6a1
Cox6a2
Coa8
Cox7a2
Coa3
Cox11
Cox18
Cox4i1
Cox5a
Cox5b
Cox7b
Coa6
Coa7
Cox20
Cox7a2l
Cox4i2
Cox7c
Cox19
Cox6b1
Cox15
Cox14
Cox16
MCT-ad libb
Control
MCT-IF
E
Complex V
Atp5mg
Atp5pb
Atp5mf
Atp5pd
Atp5po
Atp5me
Atp5pf
Atp5f1c
Atp5f1a
Mt-atp8
Atp5f1d
Atp5f1e
Atp5if1
Atp5md
MCT-ad libb
Control
MCT-IF
F
0.6507
0.0153
0.0026
Complex I Activity
(OCR/2 µg mitochondria)
250
200
150
100
50
0
Control
MCT-ad libb
MCT-IF
G
0.8171
0.0377
0.0114
Complex II Activity
(OCR/2 µg mitochondria)
150
100
50
0
Control
MCT-ad libb
MCT-IF
H
0.2570
0.7303
0.0708
Complex IV Activity
(OCR/2 µg mitochondria)
250
200
150
100
50
0
Control
MCT-ad libb
MCT-IF
I
0.2805
0.0327
0.0014
Combined Complexes I/II/IV Activity
(OCR/2 µg mitochondria)
600
400
200
0
Control
MCT-ad libb
MCT-IF

Figure 3: Correlational heatmapping identified relationships between fatty acid oxidation, electron transport chain proteins, and RV function. (A) Correlational heat map of mitochondrial fatty acid oxidation proteins and Ees/Ea. (B) *r*-value and *p*-value for each protein's relationship with Ees/Ea. Red box highlights significant relationships. (C) Correlational heat map of mitochondrial fatty acid oxidation proteins and TAPSE. (D) *r*-value and *p*-value for each protein's relationship with TAPSE. Red box highlights significant relationships. (E) Correlational heat map of peroxisomal fatty acid oxidation proteins and Ees/Ea. (F) *r*-value and *p*-value for each protein's relationship with Ees/Ea. Red box highlights significant relationships. (G) Correlational heat map of peroxisomal fatty acid oxidation proteins and TAPSE. (H) *r*-value and *p*-value for each protein's relationship with TAPSE. Red box highlights significant relationships. (I) Correlational heat map of electron transport chain proteins and Ees/Ea. (J) *r*-value and *p*-value for each protein's relationship with Ees/Ea. Red box highlights significant relationships. (K) Correlational heat map of electron transport chain proteins and TAPSE. (L) *r*-value and *p*-value for each protein's relationship with TAPSE. Red box highlights significant relationships.

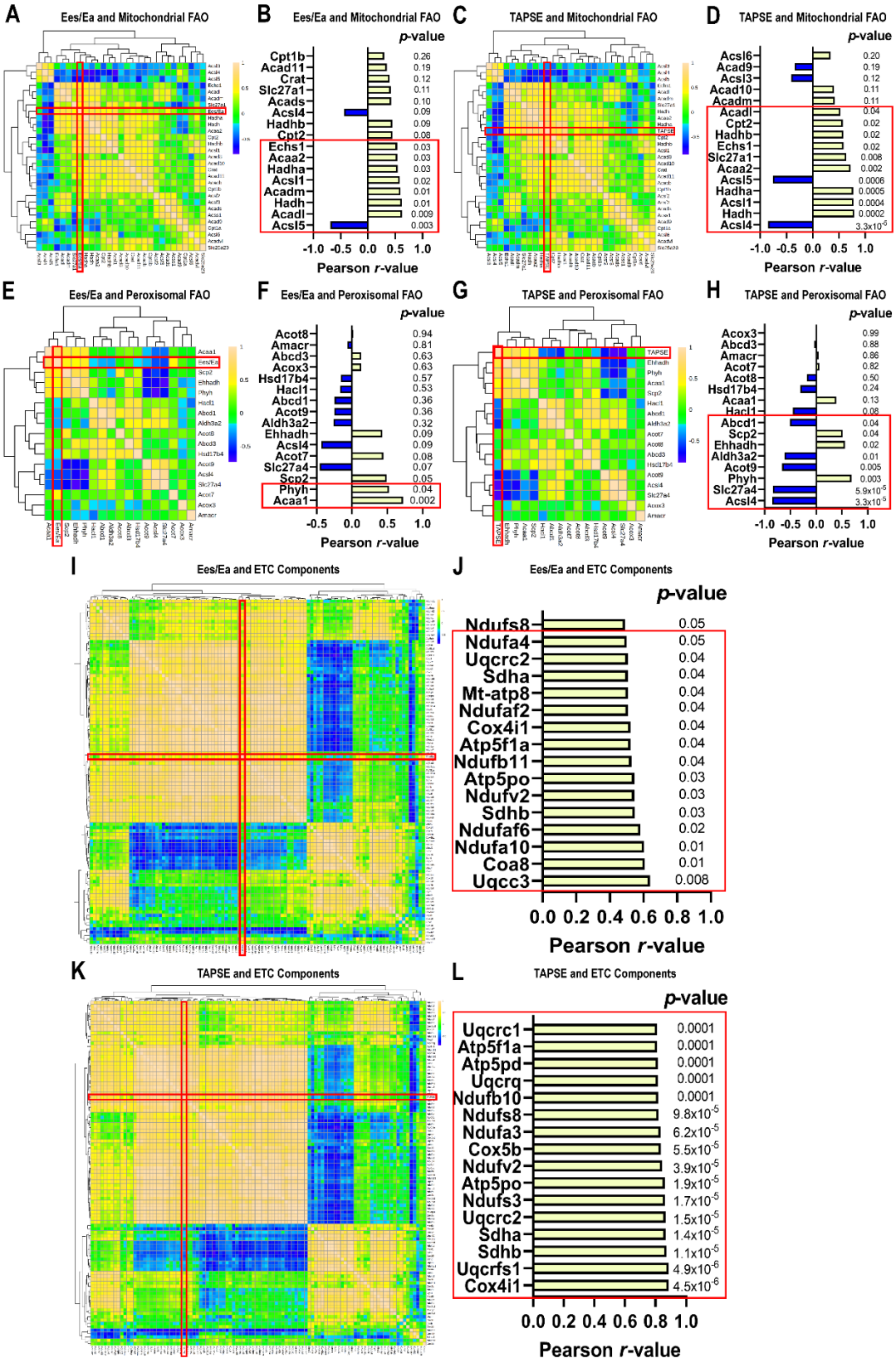
A
Ees/Ea and Mitochondrial FAO
B
Ees/Ea and Mitochondrial FAO
p-value
Cpt1b 0.26
Acad11 0.19
Crat 0.12
Slc27a1 0.11
Acads 0.10
Acsl4 0.09
Hadhb 0.09
Cpt2 0.08
Echs1 0.03
Acaa2 0.03
Hadha 0.03
Acsl1 0.02
Acadm 0.01
Hadh 0.01
Acadl 0.009
Acsl5 0.003
-1.0 -0.5 0.0 0.5 1.0
Pearson r-value
C
TAPSE and Mitochondrial FAO
D
TAPSE and Mitochondrial FAO
p-value
Acsl6 0.20
Acad9 0.19
Acsl3 0.12
Acad10 0.11
Acadm 0.11
Acadl 0.04
Cpt2 0.02
Hadhb 0.02
Echs1 0.02
Slc27a1 0.008
Acaa2 0.002
Acsl5 0.0006
Hadha 0.0005
Acsl1 0.0004
Hadh 0.0002
Acsl4 3.3x10-5
-1.0 -0.5 0.0 0.5 1.0
Pearson r-value
E
Ees/Ea and Peroxisomal FAO
F
Ees/Ea and Peroxisomal FAO
p-value
Acot8 0.94
Amacr 0.81
Abcd3 0.63
Acox3 0.63
Hsd17b4 0.57
Hacl1 0.53
Abcd1 0.36
Acot9 0.36
Aldh3a2 0.32
Ehhadh 0.09
Acsl4 0.09
Acot7 0.08
Slc27a4 0.07
Scp2 0.05
Phyh 0.04
Acaa1 0.002
-0.5 0.0 0.5 1.0
Pearson r-value
G
TAPSE and Peroxisomal FAO
H
TAPSE and Peroxisomal FAO
p-value
Acox3 0.99
Abcd3 0.88
Amacr 0.86
Acot7 0.82
Acot8 0.50
Hsd17b4 0.24
Acaa1 0.13
Hacl1 0.08
Abcd1 0.04
Scp2 0.04
Ehhadh 0.02
Aldh3a2 0.01
Acot9 0.005
Phyh 0.003
Slc27a4 5.9x10-5
Acsl4 3.3x10-5
-1.0 -0.5 0.0 0.5 1.0
Pearson r-value
I
Ees/Ea and ETC Components
J
Ees/Ea and ETC Components
p-value
Ndufs8 0.05
Ndufa4 0.05
Uqcrc2 0.04
Sdha 0.04
Mt-atp8 0.04
Ndufaf2 0.04
Cox4i1 0.04
Atp5f1a 0.04
Ndufb11 0.04
Atp5po 0.03
Ndufv2 0.03
Sdhb 0.03
Ndufaf6 0.02
Ndufa10 0.01
Coa8 0.01
Uqcc3 0.008
0.0 0.2 0.4 0.6 0.8 1.0
Pearson r-value
K
TAPSE and ETC Components
L
TAPSE and ETC Components
p-value
Uqcrc1 0.0001
Atp5f1a 0.0001
Atp5pd 0.0001
Uqcrq 0.0001
Ndufb10 0.0001
Ndufs8 9.8x10-5
Ndufa3 6.2x10-5
Cox5b 5.5x10-5
Ndufv2 3.9x10-5
Atp5po 1.9x10-5
Ndufs3 1.7x10-5
Uqcrc2 1.5x10-5
Sdha 1.4x10-5
Sdhb 1.1x10-5
Uqcrfs1 4.9x10-6
Cox4i1 4.5x10-6
0.0 0.2 0.4 0.6 0.8 1.0
Pearson r-value

Figure 4: Intermittent fasting mitigates pathological microtubule remodeling, which restores junctophilin-2 expression, and rescues t-tubule structure in RV cardiomyocytes. (A) Western blots and subsequent quantification (B) of tubulins and microtubule regulating proteins. (C) Representative confocal micrographs of microtubules in RV cardiomyocytes. (D) Quantification of relative microtubule density. IF mitigates increased microtubule density. *p*-values as determined by Kruskal-Wallis with Dunn's multiple comparisons test. (E) Representative images of RV cardiomyocyte t-tubules. (F) Quantification of t-tubule organization. *p*-values as determined by Kruskal-Wallis with Dunn's multiple comparisons test.

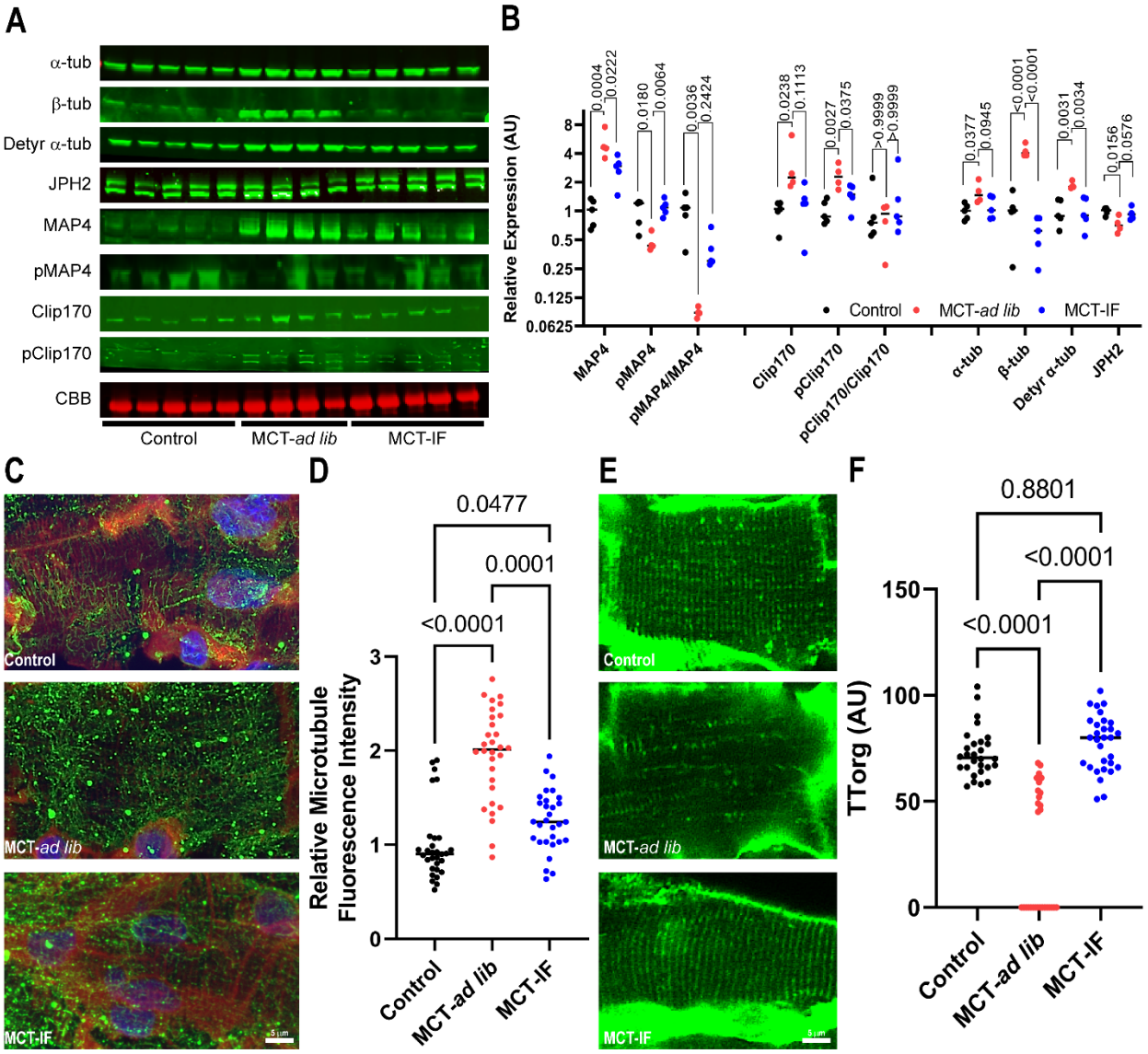

Online Methods

Animal Studies

Animals studies were performed as previously described[10]. Briefly, male Sprague Dawley rats, purchased from Charles River Laboratories, were randomized into three experimental groups: phosphate buffered saline (PBS) injected (control), monocrotaline-*ad libitum*, and monocrotaline-IF. All monocrotaline rats received a single subcutaneous injection of monocrotaline (60 mg/kg) (Sigma-Aldrich, St. Louis, MO). The monocrotaline-IF group began every other day fasting the day following monocrotaline injection. All animal studies were approved by the University of Minnesota Institutional Animal Care and Use Committee.

Western blot

Western blots were performed by probing a total of 25 µg of RV protein extract using the Odyssey Infrared Imaging system (Lincoln, NE) as previously described[15]. Post transfer SDS-PAGE gels were stained with Coomassie brilliant blue (CBB) and imaged at the 700-nm wavelength on the Odyssey Imaging System with the band corresponding to the myosin heavy chain used as the loading control[15,29].

Confocal microscopy

RV cardiomyocyte bundles from formalin fixed RV free wall specimens were manually dissected using a dissecting microscope. Bundles were subjected to antigen retrieval using Reveal Decloaker solution (Biocare Medical) for 45 minutes at 95^0C. Samples were allowed to cool to room temperature and then incubated in 1% Triton X-100 in PBS for 10 minutes. Samples were blocked in 5% goat serum in PBS for ten minutes. Primary antibodies diluted in 5% goat serum in PBS were incubated with bundles at 4^0C for 48-72 hours. Bundles were washed/blocked in 5% goat serum and then incubated with secondary antibody and Wheat Germ Agglutinin Alexa Fluor-633 conjugate (ThermoFisher) at 37^0C for 30 minutes. Samples were washed with PBS, treated with an autofluorescence quenching kit (Vector Laboratories), and then embedded in Aatifade containing DAPI (Vector Laboratories). Z-stacks of cardiomyocyte bundles were obtained with an Olympus FV1000 BX2 upright confocal microscope (Tokyo, Japan) at the University of Minnesota Imaging Center.

Quantification of mitochondrial and peroxisomal density

Cardiomyocyte bundles were stained for mitochondria or peroxisomes and then mitochondrial and peroxisome density was determined using the threshold plug-in on FIJI (Bethseda, MD). Images were blindly analyzed by FK.

Assessment of microtubule density

Cardiomyocyte bundles were stained with a β-tubulin antibody and then microtubule fluorescence intensity normalized to area was determined using FIJI (Bethseda, MD). Images were blindly analyzed by FK.

T-tubule morphological analysis

WGA staining of cardiomyocyte bundles was used to delinated t-tubules. T-tubule regularity was quantified using the TT_{Power} plug-in on FIJI. FK blindly analyzed the images.

Quantitative proteomics of mitochondrial/peroxisomal enrichments

RV mitocondrial/peroxisomal enrichments (*n*=5 control, *n*=5 MCT-*ad lib*, and *n*=6 MCT-IF) were isolated with a mitochondrial isolation kit (Abcam). Then, the mitochondrial/peroxisome pellet fraction was resuspended in lysis buffer and supplemented with protease inhibitor (ThermoFisher). The samples were briefly sonicated with a Branson Digital Sonifier 250 (Branson Ultrasonics) and then underwent pressure cycling (alternating 35 KPSI for 20 seconds and 0 KPSI for 10 seconds for 60 cycles at 37ºC). Protein concentration was determined by Bradford assay. A 25 µg aliquot of each sample was diluted in half with lysis buffer and then this sample was then diluted 5-fold with water. Trypsin (Promega) was added in a 1:40 ratio and samples were incubated overnight at 37ºC and after incubation, frozen at -80ºC and vacuum dried. Each sample was cleaned with a 1 cc Waters Oasis MCX cartridge (Waters Corporation), eluates were vacuum dried and resuspended in 100 µl of 0.1 M triethylammonium bicarbonate, pH 8.5 to a final concentration of 1 µg/µl. For each channel in the

TMT16plex, a 20 µg aliquot of the sample was made and labeled with 0.2 mg TMT16plex. Isobaric Label Reagent (Thermo Scientific). After TMT labeling, all samples were multiplexed together.

The TMT sample was then dried *in vacuo*, cleaned with a 1 cc Waters Oasis MCX solid phase extraction cartridge (Waters Corporation), and dried *in vacuo* again. The sample was resuspended in 20 mM ammonium formate, pH 10 in 98:2 water:acetonitrile and fractioned by high pH C18 reversed-phase (RP) chromatography. A Shimadzu Prominance HPLC (Shimadzu) with a Hot Sleeve 2 L Column Heater (Analytical Sales and Services, Inc.) was used with a SecurityGuard precolumn housing a Gemini NX-C18 cartridge (Phenomenex) attached to a C18 XBridge column (150 mm x 2.1 mm internal diameter, 5 µm particle size) (Waters Corporation). Buffer A was 20 mM ammonium formate, pH 10 in 98:2 water:acetonitrile and Buffer B was 20 mM ammonium formate, pH 10 in 10:90 water:acetonitrile. Flow rate was 200 µl/min with a gradient from 2-7% Buffer B over 0.5 minutes, 7-15% Buffer B over 7.5 minutes, 15-35% Buffer B over 45 minutes, and 35-60% Buffer B over 15 minutes. Fractions were collected every 2 minutes and UV absorbances were monitored at 215 and 280 nm.

Assessment of electron transport chain activity

Mitochondrial respiration was measured using frozen tissues as described in Acin-Perez *et. al*[18]. Briefly, snap-frozen RV tissue, stored at -80, was place in a 2 mL Kontes glass homogenizer with 200ul of MAS buffer then minced with a scissors. The tissue was homogenized with 20 strokes of pestle B (0.0005 inch clearance). Based on BCA assay (Thermo Scientific) standard curves, approximately 2ug was assayed per well of 96 well Agilent cell culture dishes (Agilent). The plate was run on an Agilent XFe96 Seahorse analyzer. Data was exported to Xcel and analyzed in GraphPad Prism.

Echocardiography

Echocardiography was completed with a Vevo2100 ultrasound system at the University of Minnesota Imaging Center. M-mode images were used to measure tricuspid annular plane systolic excursion.

Closed-chest pressure-volume hemodynamic studies

5% inhaled isoflurane was used for induction and then rats were maintained on 2-3% isoflurane while they were ventilated with a SomnoSuite small animal anesthesia system (Kent Scientific, Torrington, CT). A high-fidelity catheter (Scisense 1.9F pressure-volume, Transonic Systems, Ithaca, NY) was placed into the RV via the right internal jugular vein. RV pressure and volume were measured with the Transonic AV500 Pressure-Volume Measurement System and then analyzed on LabScribe version 4 (iWorx Systems, Dover, NH) as we have previously described[7,10,19].

Statistics

Statistical analyses were performed with GraphPad Prism 9.0 (San Diego, CA). Normality of data was determined by Shapiro-Wilk test. If data was normally distributed and there was equal variance as determined by the Brown-Forsythe test, one-way analysis of variance (ANOVA) with Tukey's multiple comparisons test was performed. If there was unequal variance, Brown-Forsythe and Welch ANOVA with Dunnett multiple comparisons test was completed. If the data was not normally distributed, Kruskal-Wallis test and Dunn's multiple comparisons test was used. Graphs show the mean value and all individual values.

Hierarchical cluster analyses and correlational heatmapping were performed with MetaboAnalyst software[30]. Relative abundance of each protein in proteomics studies was determined with Scaffold Software and those values were used for both analyses.

Supplemental Table 1: Antibodies and Dilutions Used in Study

Antigen	Company	Catalogue Number	Dilution	Experimental Approach
AMP kinase	Cell Signaling Technology	2532	1:200	Western blot
Phosphorylated AMP kinase	Cell Signaling Technology	2531	1:200	Western blot
α-tubulin	Millipore	05-829	1:250	Western blot
β-tubulin	Sigma-Aldrich	T4026	1:250	Western blot
Detyrosinated α-tubulin	Abcam	ab48389	1:250	Western blot
MAP4	Millipore	ab6020	1:100	Western blot
Phosphorylated MAP4	Thermo Scientific	B5-5438R	1:100	Western blot
CLIP-170	Cell Signaling Technology	8977S	1:250	Western blot
Phosphorylated CLIP-170	Kind gift from Dr. Yasunori Shintani	Not applicable	1:250	Western blot
Junctophilin-2	Thermo Fisher Scientific	A304-455A	1:250	Western blot
β-tubulin	Abcam	Ab6046	1:50	Immunofluorescence
Catalase	Abcam	Ab209211	1:50	Immunofluorescence
Mitofusin-2	Abnova	H00009927-M01	1:50	Immunofluorescence
Anti-rabbit Alexa 555 secondary antibody	Invitrogen	A32732	1:500	Immunofluorescence
Anti-mouse secondary	Li-COR	926-32210 926-68070	1:5000	Western blot
Anti-rabbit secondary	Li-COR	926-32211 926-68071	1:5000	Western blot

Supplemental Figure 1: **Ferroptosis proteins are dysregulated in RV failure and pro-ferroptotic proteins are associated with depressed RV function.** (A) Hierarchical cluster analysis of ferroptosis proteins. MCT-*ad lib* RVs had higher levels of pro-ferroptotic proteins, which was mitigated by IF. (B) Correlational heat map of ferroptotic proteins and Ees/Ea. (C) *r*-value and *p*-value for each protein's relationship with Ees/Ea. Red box highlights significant relationships. (D) Correlational heat map of ferroptotic proteins and TAPSE. (E) *r*-value and *p*-value for each protein's relationship with TAPSE. Red box highlights significant relationships.

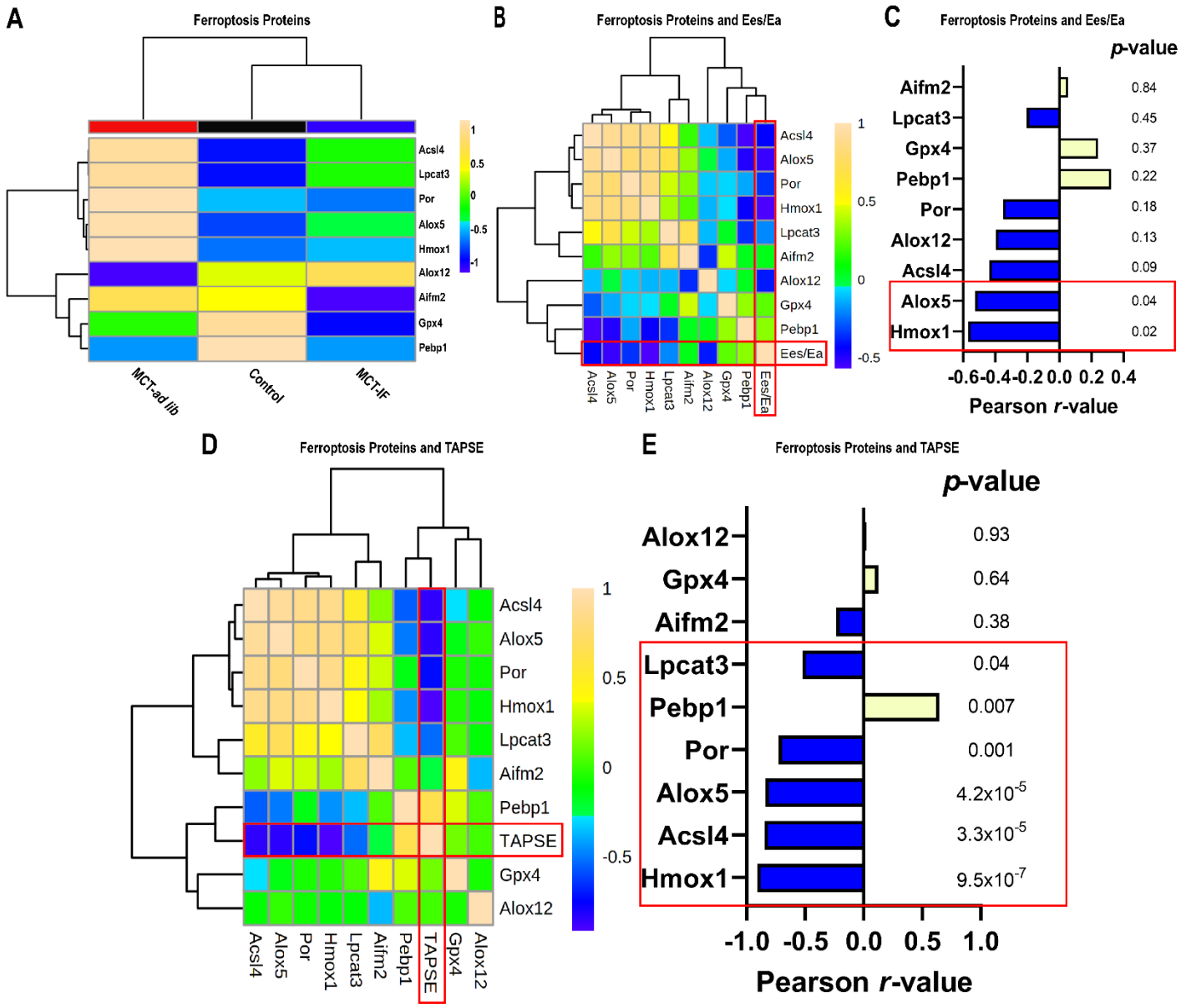

Supplemental Figure 2: Peroxisomal-mediated ferroptosis proteins are upregulated in RV failure and inversely associated with RV function. (A) Hierarchical cluster analysis of ferroptosis proteins. MCT-*ad lib* RVs had higher levels of nearly all peroxisomal-mediated ferroptotic proteins, which was mitigated by IF. (B) Correlational heat map of peroxisomal-mediated ferroptotic proteins and Ees/Ea. (C) *r*-value and *p*-value for each protein's relationship with Ees/Ea. Red box highlights significant relationships. (D) Correlational heat map of peroxisomal-mediated ferroptotic proteins and TAPSE. (E) *r*-value and *p*-value for each protein's relationship with TAPSE. Red box highlights significant relationships.

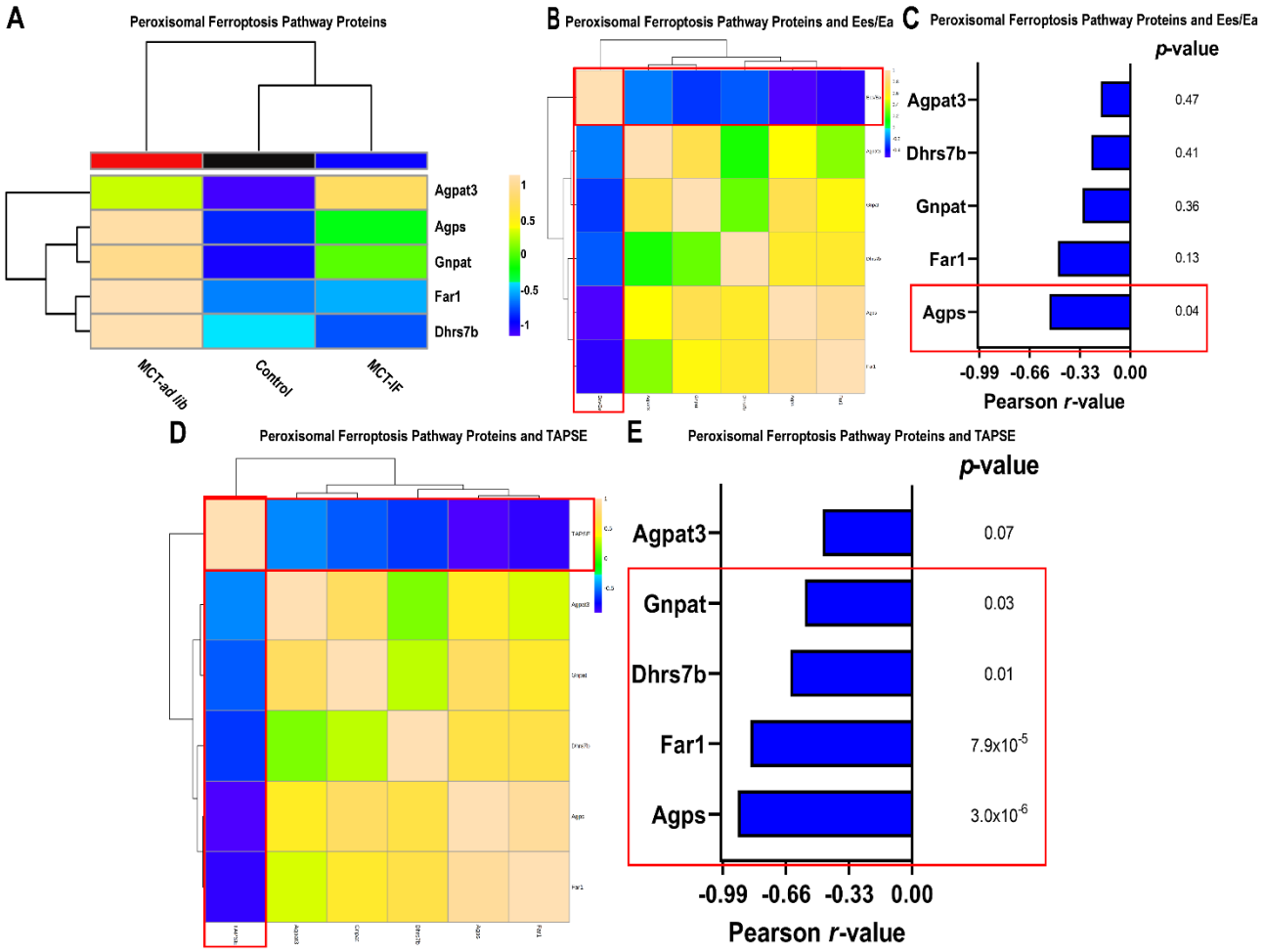

Supplemental Figure 3: Quantification of Ees/Ea (A) and TAPSE (B) in animals that were analyzed in proteomics experiments. *p*-values as determined by one-way ANOVA with Tukey's multiple comparisons test.

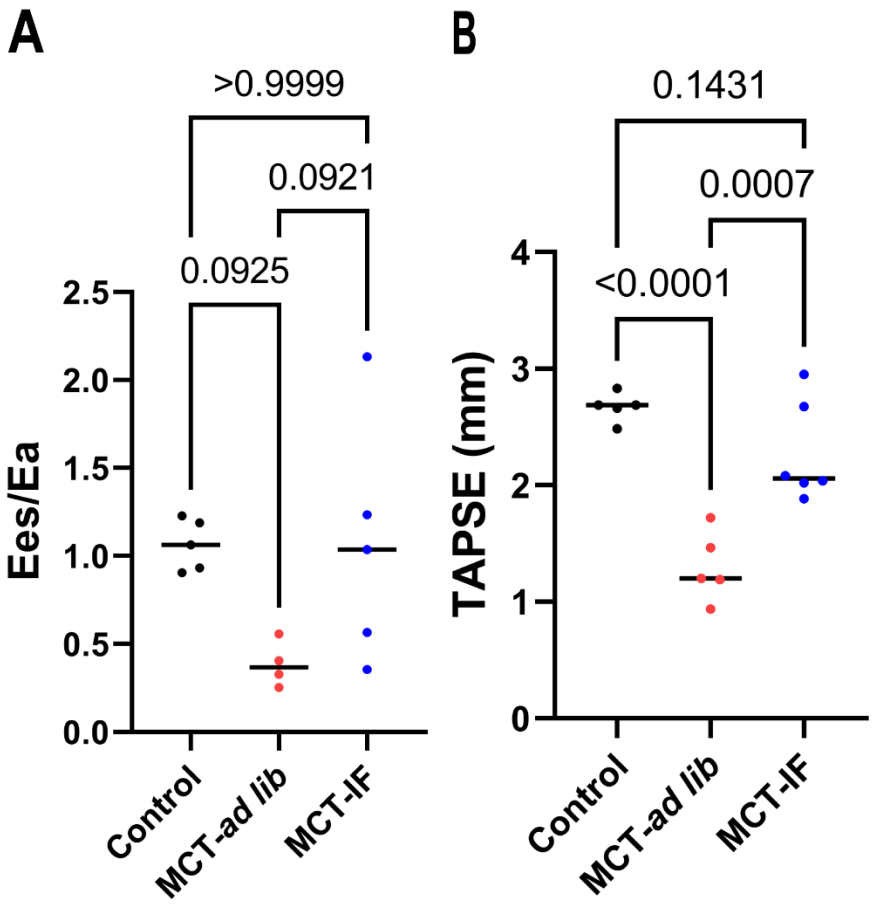

References

1 Patterson, R. E. & Sears, D. D. Metabolic Effects of Intermittent Fasting. *Annu Rev Nutr* **37**, 371-393, doi:10.1146/annurev-nutr-071816-064634 (2017).

2 de Cabo, R. & Mattson, M. P. Effects of Intermittent Fasting on Health, Aging, and Disease. *N Engl J Med* **381**, 2541-2551, doi:10.1056/NEJMra1905136 (2019).

3 Weir, H. J. *et al.* Dietary Restriction and AMPK Increase Lifespan via Mitochondrial Network and Peroxisome Remodeling. *Cell Metab* **26**, 884-896.e885, doi:10.1016/j.cmet.2017.09.024 (2017).

4 Prisco, S. Z., Thenappan, T. & Prins, K. W. Treatment Targets for Right Ventricular Dysfunction in Pulmonary Arterial Hypertension. *JACC Basic Transl Sci* **5**, 1244-1260, doi:10.1016/j.jacbts.2020.07.011 (2020).

5 Agrawal, V., Lahm, T., Hansmann, G. & Hemnes, A. R. Molecular mechanisms of right ventricular dysfunction in pulmonary arterial hypertension: focus on the coronary vasculature, sex hormones, and glucose/lipid metabolism. *Cardiovasc Diagn Ther* **10**, 1522-1540, doi:10.21037/cdt-20-404 (2020).

6 Hemnes, A. R. *et al.* Evidence for right ventricular lipotoxicity in heritable pulmonary arterial hypertension. *Am J Respir Crit Care Med* **189**, 325-334, doi:10.1164/rccm.201306-1086OC (2014).

7 Prisco, S. Z., Eklund, M., Raveendran, R., Thenappan, T. & Prins, K. W. With No Lysine Kinase 1 Promotes Metabolic Derangements and RV Dysfunction in Pulmonary Arterial Hypertension. *JACC Basic Transl Sci* **6**, 834-850, doi:10.1016/j.jacbts.2021.09.004 (2021).

8 Brittain, E. L. *et al.* Fatty Acid Metabolic Defects and Right Ventricular Lipotoxicity in Human Pulmonary Arterial Hypertension. *Circulation* **133**, 1936-1944, doi:10.1161/CIRCULATIONAHA.115.019351 (2016).

9 Bikman, B. T. & Summers, S. A. Ceramides as modulators of cellular and whole-body metabolism. *J Clin Invest* **121**, 4222-4230, doi:10.1172/JCI57144 (2011).

10 Prisco, S. Z. *et al.* Intermittent Fasting Enhances Right Ventricular Function in Preclinical Pulmonary Arterial Hypertension. *J Am Heart Assoc* **10**, e022722, doi:10.1161/JAHA.121.022722 (2021).

11 Fassett, J. T. *et al.* AMPK attenuates microtubule proliferation in cardiac hypertrophy. *Am J Physiol Heart Circ Physiol* **304**, H749-758, doi:10.1152/ajpheart.00935.2011 (2013).

12 Yashirogi, S. *et al.* AMPK regulates cell shape of cardiomyocytes by modulating turnover of microtubules through CLIP-170. *EMBO Rep* **22**, e50949, doi:10.15252/embr.202050949 (2021).

13 Uchida, K., Scarborough, E. A. & Prosser, B. L. Cardiomyocyte Microtubules: Control of Mechanics, Transport, and Remodeling. *Annu Rev Physiol* **84**, 257-283, doi:10.1146/annurev-physiol-062421-040656 (2022).

14 Caporizzo, M. A., Chen, C. Y. & Prosser, B. L. Cardiac microtubules in health and heart disease. *Exp Biol Med (Maywood)* **244**, 1255-1272, doi:10.1177/1535370219868960 (2019).

15 Prins, K. W. *et al.* Colchicine Depolymerizes Microtubules, Increases Junctophilin-2, and Improves Right Ventricular Function in Experimental Pulmonary Arterial Hypertension. *J Am Heart Assoc* **6**, doi:10.1161/JAHA.117.006195 (2017).

16 Zhang, C. *et al.* Microtubule-mediated defects in junctophilin-2 trafficking contribute to myocyte transverse-tubule remodeling and Ca2+ handling dysfunction in heart failure. *Circulation* **129**, 1742-1750, doi:10.1161/CIRCULATIONAHA.113.008452 (2014).

17 Lopaschuk, G. D., Karwi, Q. G., Tian, R., Wende, A. R. & Abel, E. D. Cardiac Energy Metabolism in Heart Failure. *Circ Res* **128**, 1487-1513, doi:10.1161/CIRCRESAHA.121.318241 (2021).

18 Acin-Perez, R. *et al.* A novel approach to measure mitochondrial respiration in frozen biological samples. *EMBO J* **39**, e104073, doi:10.15252/embj.2019104073 (2020).
19 Prisco, S. Z. *et al.* Inflammatory Glycoprotein 130 Signaling Links Changes in Microtubules and Junctophilin-2 to Altered Mitochondrial Metabolism and Right Ventricular Contractility. *Circ Heart Fail* **15**, e008574, doi:10.1161/CIRCHEARTFAILURE.121.008574 (2022).
20 Doll, S. *et al.* ACSL4 dictates ferroptosis sensitivity by shaping cellular lipid composition. *Nat Chem Biol* **13**, 91-98, doi:10.1038/nchembio.2239 (2017).
21 Beatty, A. *et al.* Ferroptotic cell death triggered by conjugated linolenic acids is mediated by ACSL1. *Nat Commun* **12**, 2244, doi:10.1038/s41467-021-22471-y (2021).
22 Li, J. *et al.* Ferroptosis: past, present and future. *Cell Death Dis* **11**, 88, doi:10.1038/s41419-020-2298-2 (2020).
23 Schmid, E. *et al.* Cardiac RKIP induces a beneficial β-adrenoceptor-dependent positive inotropy. *Nat Med* **21**, 1298-1306, doi:10.1038/nm.3972 (2015).
24 Lee, H. *et al.* Energy-stress-mediated AMPK activation inhibits ferroptosis. *Nat Cell Biol* **22**, 225-234, doi:10.1038/s41556-020-0461-8 (2020).
25 Fang, X. *et al.* Ferroptosis as a target for protection against cardiomyopathy. *Proc Natl Acad Sci U S A* **116**, 2672-2680, doi:10.1073/pnas.1821022116 (2019).
26 Tadokoro, T. *et al.* Mitochondria-dependent ferroptosis plays a pivotal role in doxorubicin cardiotoxicity. *JCI Insight* **5**, doi:10.1172/jci.insight.132747 (2020).
27 Zou, Y. *et al.* Plasticity of ether lipids promotes ferroptosis susceptibility and evasion. *Nature* **585**, 603-608, doi:10.1038/s41586-020-2732-8 (2020).
28 Cignarella, F. *et al.* Intermittent Fasting Confers Protection in CNS Autoimmunity by Altering the Gut Microbiota. *Cell Metab* **27**, 1222-1235.e1226, doi:10.1016/j.cmet.2018.05.006 (2018).
29 Prins, K. W., Asp, M. L., Zhang, H., Wang, W. & Metzger, J. M. Microtubule-Mediated Misregulation of Junctophilin-2 Underlies T-Tubule Disruptions and Calcium Mishandling in mdx Mice. *JACC Basic Transl Sci* **1**, 122-130, doi:10.1016/j.jacbts.2016.02.002 (2016).
30 Chong, J., Yamamoto, M. & Xia, J. MetaboAnalystR 2.0: From Raw Spectra to Biological Insights. *Metabolites* **9**, doi:10.3390/metabo9030057 (2019).